Design and Analysis of a Sub-THz Resonator-Based High-Resolution Permittivity Sensor

Hai Yu, *Member, IEEE*, Xuan Ding, *Member, IEEE*, Jingjun Chen, *Member, IEEE*, Sajjad Sabbaghi, *Graduate Student Member, IEEE*, and Qun Jane Gu, *Senior Member, IEEE*

***Abstract*— In this work, we propose a high-resolution CMOS permittivity sensor integrated with a high-Q whispering gallery mode (WGM) resonator at sub-THz frequencies. The system compares the transmission coefficients of a pair of WGM resonator sensors to detect small complex permittivity difference of the sensing and the reference material under test (MUT). A sub-THz voltage-controlled oscillator (VCO) in the transmitter (TX) generates the excitation signal for sensing. The TX noise is suppressed by injection locking the receiver (RX) through the sub-THz local oscillator (LO) feedforward path. The low-frequency noises are suppressed by a BPSK chopping scheme, and the high-frequency noises are reduced by windowed integration. Detailed analog signal processing analysis provides design insights into noise reduction. The WGM sensor is fabricated in house with lithography, and the CMOS transceiver (TRX) is implemented in a 28-nm CMOS technology. The boosted sensitivity by the WGM sensor and the multifold noise reduction enable the sensing system to achieve a record permittivity sensing resolution of 0.05% with an integration time of 14 μs and a power consumption of 54 mW.**

***Index Terms*— Active mixer, chopping, CMOS, coherent phase noise cancellation (CPNC), flicker noise reduction, Gm-C integrator, injection locking, millimeter wave, permittivity sensing, resonator sensor, sub-THz, voltage-controlled oscillator (VCO), whispering gallery mode (WGM) resonator.**

I. Introduction

PERMITTIVITY sensing has wide applications in a variety of industries, such as petroleum, agriculture, food production, and so on [1]. The complex permittivity serves as an effective indicator of the valuable information of the sample material, such as their constitute, moisture, or quality, which are critical in the process of product development, production, and treatment. The nondestructive nature of the permittivity sensing makes it highly cost-effective and enables it for real-time material characterization [2], [3]. This calls for the adoption of CMOS technologies to achieve a high level of integration of signal processing capabilities for cost-effective and ubiquitous applications without sacrificing precision and accuracy. Therefore, numerous works featuring CMOS permittivity sensor have been developed [4], [5], [6], [7] [8], [9], [10], [11].

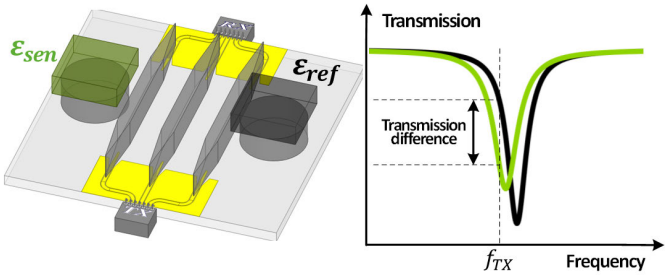

Fig. 1. 3-D view of the sensing system and the illustration of the sensing mechanism.

Among all aspects of CMOS permittivity sensing systems, high-resolution sensing is of particular importance, which enables CMOS sensing in applications, such as high-precision biosensing, precision medicine, and so on. High-resolution sensing enables high-throughput measurement [10], capturing fast process in real time. To achieve high resolution, the prior art focuses on two key aspects: permittivity sensor's sensitivity boost and system noise reduction. In [12], a meta-material-based sensor structure is proposed to boost the sensor's sensitivity comparing with conventional transmission line-based sensors. In [13], rail-to-rail square wave signaling is utilized to improve the sensitivity of the transmission line-based delay sensor.

In the optical community, on the other hand, ultrahigh sensitivity is achieved by utilizing resonator-based sensors, whose resonant frequency is shifted by the permittivity of different material under tests (MUTs) [14]. Sharp curvature and steep slope of the transmission coefficient of the high-Q resonator sensors result in high sensitivity. Whispering gallery mode (WGM) resonators show particularly high sensitivity due to its high Q and the strong field interaction with the MUTs [15]. However, the expensive and bulky tunable optical sources and the limited signal processing and readout capabilities severely constrain the applications of the high-sensitivity optical sensors.

To advance the state of the arts of the high-resolution permittivity sensors, we demonstrated a sub-THz WGM resonator-based CMOS permittivity sensor [16]. Because of its short wavelength, the WGM resonator sensor at sub-THz possesses a compact form factor, achieving a high level of integration with the CMOS transceivers (TRXs). Similar to

Manuscript received 23 September 2023; revised 15 December 2023; accepted 11 January 2024. Date of publication 9 February 2024; date of current version 7 May 2024. This work was supported in part by the National Science Foundation (NSF). This paper is an expanded version from the IEEE RFIC Symposium, San Diego, CA, USA, June 11–13, 2023. *(Corresponding author: Hai Yu.)*

The authors are with the Department of Electrical and Computer Engineering, University of California at Davis, Davis, CA 95616 USA (e-mail: jetyu@ucdavis.edu).

Color versions of one or more figures in this article are available at https://doi.org/10.1109/TMTT.2024.3357594.

Digital Object Identifier 10.1109/TMTT.2024.3357594

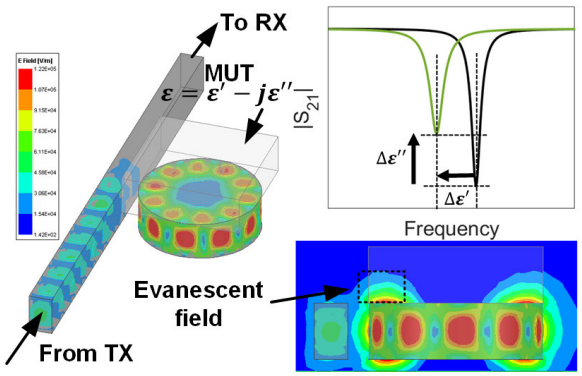

Fig. 2. WGM sensor mechanism.

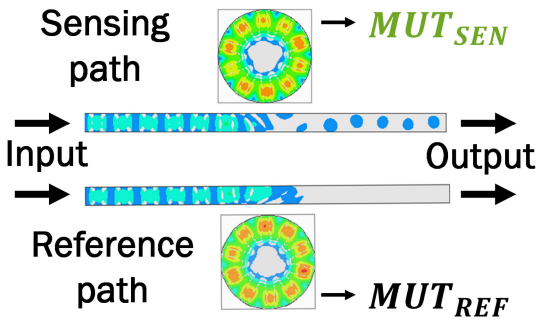

Fig. 3. Complementary sensing and reference paths.

its optical counterparts [17], the compactness of the sub-THz sensor also enables high-sensitivity detection while requiring a smaller amount of MUT samples than sensors working at GHz frequency range. As shown in Fig. 1, the sensor compares the transmission coefficients of a pair of WGM disk resonator sensors to detect small complex permittivity difference of the sensing and reference MUTs. A sub-THz voltage-controlled oscillator (VCO) in transmitter (TX) generates the excitation signal to the sensing and reference sensors. The TX noise is suppressed by injection locking the receiver (RX)'s local oscillator (LO) through the sub-THz LO feedforward path. The low-frequency noises are suppressed by a BPSK chopping scheme, and the high-frequency noises are reduced by windowed integration. The boosted sensitivity by the WGM sensor and the multifold noise reduction enable this sensing system to achieve a record sensing resolution with a short integration time and low-power consumption comparing with prior arts. Expanded from [16], this article provides innovative design details, signal and noise analysis at system level, more simulation and measurement results, and detailed analog signal processing analysis that provides design insights for noise reduction. This article is organized as follows. The mechanism and the implementation of the sub-THz WGM resonator sensor are described in Section II. The proposed sensing system structure is presented in Section III, with detailed system-level signal and noise analysis. In Section IV, circuit design details and simulation results are presented. Section V presents the measurement results and performance of the proposed sensing system and compares with the state of the arts. After the conclusion in Section VI and acknowledgment, two appendix sections collect the key steps of the derivation of the flicker noise reduction and windowed integration analysis.

II. WGM Sensor Mechanism, Design, and Implementation

The working mechanism of a single WGM resonator sensor is shown in Fig. 2. The sub-THz signal is sent from the TX to the RX through the dielectric waveguide [18]. The disk resonator couples and dissipates power from the waveguide at its resonant frequency, therefore forming a transmission notch. The evanescent field extends out from the dielectric resonator and interacts with the dielectric MUT placed on top of the disk resonator. The complex permittivity of the MUT can be expressed as $\epsilon = \epsilon' - j\epsilon''$. Also, it is often convenient to use the relative permittivity $\epsilon_r = \epsilon/\epsilon_0 = \epsilon_r' - j\epsilon_r''$, which is the permittivity normalized to the vacuum permittivity ϵ_0. The real and imaginary parts of the permittivity of the MUT indicate its electric energy storing (reactive) capability and its loss (resistive) property, respectively, and therefore, they change the transmission notch of the resonator sensor in different manners. The real permittivity ϵ' changes the center frequency of the transmission notch by changing the resonant frequency of the resonator. The resonant frequency f_{res} is determined by

$$f_{\text{res}} = \frac{Nc}{2\pi r_{\text{eff}}\sqrt{\epsilon'_{\text{eff}}}} \tag{1}$$

where N is the number of wavelengths in the resonator (or the mode number) and c is the speed of light in vacuum. r_{eff} is the circulating radius of the resonant mode, which dependents on the radius of the resonator disk. ϵ'_{eff} is the effective real permittivity of the resonator, which is determined by the disk material and its proximate dielectric environment. The MUTs with higher real permittivity result in a higher ϵ'_{eff} and, in turn, lead to a lower resonant frequency, as shown in Fig. 2. The imaginary permittivity ϵ'' changes the depth of the transmission notch by changing the power dissipation of the resonator. MUT with higher ϵ'' has higher loss and dissipates more power from the resonator, which results in shallower transmission notch in the undercoupling condition [19].

Two identical resonator sensors form a complementary pair of the sensing and reference paths, as shown in Fig. 3. When a reference material is placed on the sensor of the reference path, and an unknown material is placed on the sensor of the sensing path, the transmission difference, $\Delta S_{21} = S_{21,\text{SEN}} - S_{21,\text{REF}}$, reflects the permittivity difference of the two material. Fig. 4 shows exemplified simulation results of ΔS_{21} for the different scenarios (color coded) when the real and/or the imaginary permittivity of the two materials are different. In these examples, the reference material remains the same, which has a relative permittivity of $\epsilon_r = 2 - j0.001$. When the material on the sensing path has a 0.5 higher ϵ_r' than the reference material, the transmission notch shifts to lower frequencies, as shown in Fig. 4(a). The resulting transmission difference ΔS_{21} waveform manifests as an odd function around the middle of the two resonant frequencies, as shown in Fig. 4(b). The peak–peak amplitude of the waveform, $\Delta S_{21,pp,\Delta\epsilon_r'}$, is proportional to the real permittivity difference and is about 0.48 when $\Delta\epsilon_r' = 0.5$. In another scenario, when

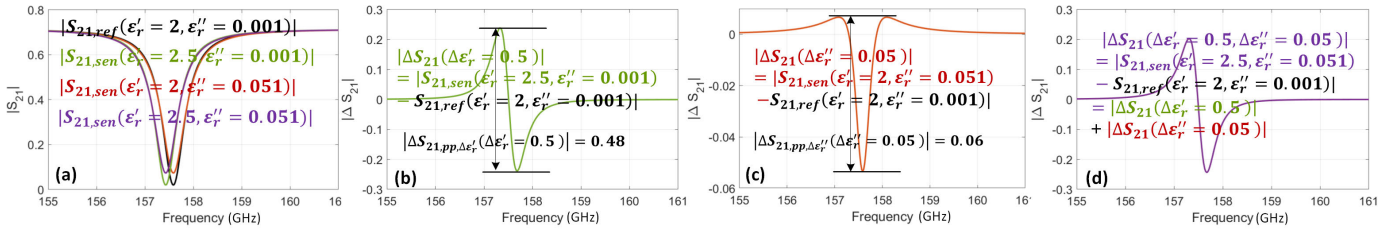

Fig. 4. Complex permittivity sensing mechanism. (a) Sensor transmission for a reference material and for three other materials with different permittivities. (b) Sensor transmission difference of materials with only real permittivity difference. (c) Sensor transmission difference of materials with only imaginary permittivity difference. (d) Sensor transmission difference of materials with both real and imaginary permittivity difference.

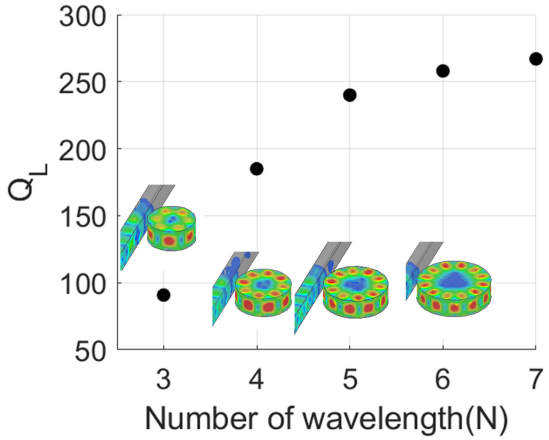

Fig. 5. Q versus number of wavelengths of the resonating WGM.

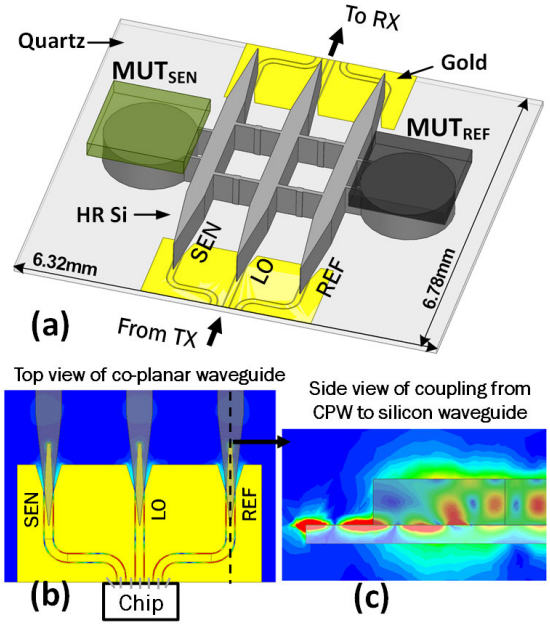

Fig. 6. Sensor structure implementation. (a) 3-D view of the whole sensor structure. (b) Top view of the CPW-dielectric waveguide coupler. (c) Side view of the CPW-dielectric waveguide coupler and E-field of the TEM mode in the CPW coupling to the E_y11 mode in the dielectric waveguide.

the material on the sensing path has a 0.05 higher ϵ_r'' than the reference material, the depth of the transmission notch elevates to a shallower level, as shown in Fig. 4(a). The resulting transmission difference ΔS_{21} waveform manifests as an even function around the resonant frequency, as shown in Fig. 4(c). The peak–peak amplitude of the waveform, $\Delta S_{21,pp,\Delta\epsilon_r''}$, proportional to the imaginary permittivity difference, is 0.06 when $\Delta\epsilon_r'' = 0.05$. When both the real and imaginary parts of the permittivity of the sensing material are different from the reference material, for example, $\Delta\epsilon_r = 0.5 - j0.05$; both the frequency and the depth of the notch show changes, as shown in Fig. 4(a). The resultant ΔS_{21} waveform is shown in Fig. 4(d). Also, the waveform in Fig. 4(d) is also the superposition of the waveforms of Fig. 4(b) and (c). This gives the WGM resonator sensor the capability of complex permittivity sensing based on the measured transmission difference waveforms.

The real permittivity sensitivity $\text{Sen}_{\epsilon_r'}$ and imaginary permittivity sensitivity $\text{Sen}_{\epsilon_r''}$ of the sensor are defined as follows:

$$\text{Sen}_{\epsilon_r'} \stackrel{\text{def}}{=} \frac{|\Delta S_{21,pp,\Delta\epsilon_r'}|}{\Delta\epsilon_r'}, \quad \text{Sen}_{\epsilon_r''} \stackrel{\text{def}}{=} \frac{|\Delta S_{21,pp,\Delta\epsilon_r''}|}{\Delta\epsilon_r''} \tag{2}$$

where $\Delta\epsilon_r'$ and $\Delta\epsilon_r''$ are the real and imaginary permittivities difference between the reference and sensing materials that cause the corresponding waveform amplitudes $|\Delta S_{21,pp,\Delta\epsilon_r'}|$ and $|\Delta S_{21,pp,\Delta\epsilon_r''}|$. The sensitivities are optimized when the resonators have high Q and are near critical coupling with the feeding waveguide, so that the steep slope and sharp curvature near the resonance produce large response even with small $\Delta\epsilon_r'$ and $\Delta\epsilon_r''$. While critical coupling is achieved by adjusting the gap between the disk and the waveguide, Q can be improved by increasing the radius of the disk. When the disk radius is small, the bend loss of the traveling wave inside the disk resonator is higher, due to the higher curvature of the outer surface. Therefore, to obtain higher Q, disk with larger radius is preferred. Fig. 5 shows the simulated Q for different numbers of wavelengths in the resonator. $N = 5$, which corresponds to a disk radius of 775 μm, is chosen to balance the Q and the sensor size. The resultant Q is 246, which leads to the permittivity sensitivity of $\text{Sen}_{\epsilon_r'} = 0.96$ and $\text{Sen}_{\epsilon_r''} = 1.2$. For conciseness, the system analysis in the rest of this article is based on ϵ_r, which is a representation of either ϵ_r' or ϵ_r'' without loss of specificity. For example, Sen_{ϵ_r} in (3) can represent either $\text{Sen}_{\epsilon_r'}$ or $\text{Sen}_{\epsilon_r''}$.

The finalized sensor structure is shown in Fig. 6. The waveguides and the sensors of the sensing path, reference path, and the waveguide of an LO feedforward path are made by high-resistivity Si (HR-Si) and are held by thin arms into one piece to facilitate the fabrication and packaging. Using a flip-chip bonder Fineplacer by Finetech, the three paths of the Si sensor structure are aligned with the coplanar waveguides (CPWs) on a quartz substrate of 100-μm thickness, and the Si sensor structure is then glued on the substrate. The

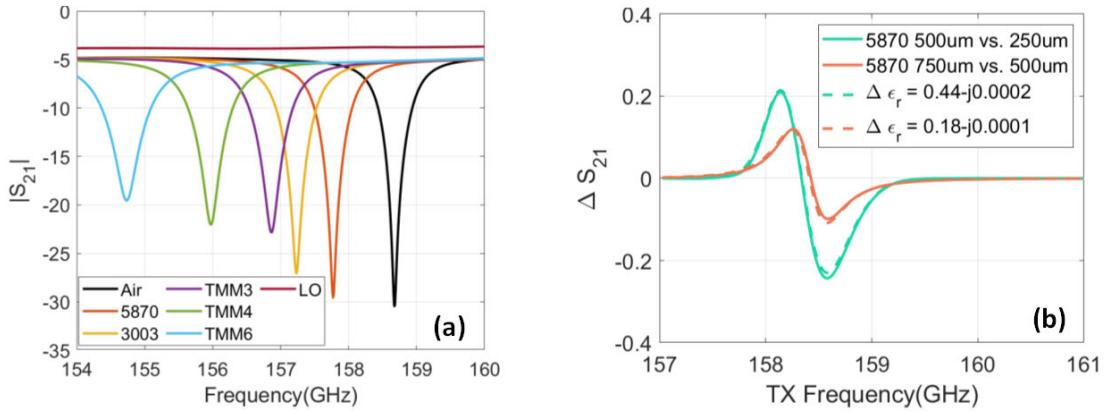

Fig. 7. Simulation results of the sensor structure. (a) S_{21} of LO and the sensing path when various Rogers laminate MUT samples placed on the sensor ($\epsilon_{r,5870} = 2.33 - j0.0005$, $\epsilon_{r,3003} = 3 - j0.0011$, $\epsilon_{r,\text{TMM3}} = 3.45 - j0.002$, $\epsilon_{r,\text{TMM4}} = 4.7 - j0.002$, and $\epsilon_{r,\text{TMM6}} = 6.3 - j0.0023$). (b) Transmission difference of Rogers 5870 with different thicknesses and equivalent permittivity difference.

signals are coupled from the CPW on the quartz substrate by the near-field CPW-dielectric waveguide coupler. Also, the CPWs are connected to the TRX chip through bonding wires. The simulated transmission of the complete sensor structure with different sample materials on the sensor is shown in Fig. 7(a). With the sensing and the reference path being identical, only the transmission of the sensing path is shown. The 250-μm-thick Rogers laminate samples are used as MUTs. The horizontal dimensions of the MUTs are 2 $\times$ 2 mm, to ensure full coverage of the sensor disk, as shown in Fig. 6(a). As shown in Fig. 7(a), to measure dielectric material with $\epsilon' < 6$, the operation frequency range requirement for the TRX IC is 6 GHz. Also, the LO path has an insertion loss of 4 dB, with 1.6-dB loss coming from the coupler of each side. As also shown in Fig. 7(a), the Q of the sensor drops for MUT with larger ϵ'_r. Higher ϵ'_r of the MUT lowers the ϵ'_r contrast at the boundary between the sensor and the MUT, leading to less field confinement in the sensor and resulting in higher loss and, hence, lower Q. Also, higher ϵ''_r directly lowers the Q of the resonator. The resultant lowered sensitivity leads to worse resolution, as shown in (12) at the bottom of the page 8. From simulation, a permittivity range of $\epsilon'_r = 1-6$ and $\epsilon''_r = 0 - 0.1$ ensures a system resolution better than 0.1%.

The MUT sample's thickness can also affect the transmission. Thicker sample of the same material allows more evanescent field to extend from the resonator sensor to the sample, therefore changing the effective permittivity experienced by the resonator. Fig. 7(b) shows the simulated transmission difference of the sensing and the reference path when Rogers 5870 samples with different thicknesses are placed on the sensing and the reference paths. The transmission difference caused by the different thicknesses of the same material type can be equivalent to certain permittivity difference of material samples with the same thickness. Furthermore, it is observed from simulation that, when the sample thickness exceeds 1 mm, however, the sensor is insensitive to sample thickness variation. This is because the evanescent field decays fast inside the sample, and there is negligible field above the height of 1 mm. Therefore, for accurate permittivity measurement, the sample should be prepared to have a thickness larger than 1 mm. On the other hand, the sensor is insensitive to the horizontal dimensions of the MUT samples as long as the sample covers the entire top surface of the sensor disk. The sensor structure is fabricated in-house in the university cleanroom through lithography and deep silicon etching.

There are two potential nonidealities for the sensor structure. The first is the cross coupling of the three paths due to their proximity to each other in the CPW section. The coupling between the LO and sensing/reference paths is around -26 dB, and the coupling between the sensing and the reference is around -55 dB. As can be seen from the signal analysis in Section III, due to the differential signaling of the sensing and reference paths, the -55 dB results in a negligible signal and, therefore, SNR weakening. The LO signal coupling to the sensing and reference path manifests as a dc offset after mixing with itself at the RX mixer and will be canceled by the baseband chopper. The second nonideality is the mismatch between the sensing and the reference paths, caused by the nonuniform etching gradient in the deep silicon etching procedure. This results in a 50-MHz resonant frequency difference of the two paths even identical MUTs are placed on the two paths. However, this static mismatch can be calibrated out in the measurement procedure, as can be seen in Section V.

III. System Architecture and SNR Analysis

A. System Architecture

Fig. 8 shows the system architecture, and Fig. 9 illustrates the signal and noise in frequency domain at critical nodes. The TX outputs a complementary pair of BPSK-modulated sub-THz signals through two identical off-chip silicon WGM disk resonator sensors near their band-stop resonant frequency, which are then summed by the combiner of the RX. The resulting signal reflects the transmission difference ΔS_{21} between the sensing and the reference path, which is then downconverted by the RX mixer. The proceeding chopper upconverts the low-frequency noise, and the following integrator filters out the high-frequency noise.

As shown in Fig. 9, the TX chopper modulates the carrier generated by the VCO into BPSK signal at a chopping frequency of $\omega_{\text{CHOP}} = 10$ MHz. The higher harmonics of the BPSK modulation are omitted in this qualitative figure

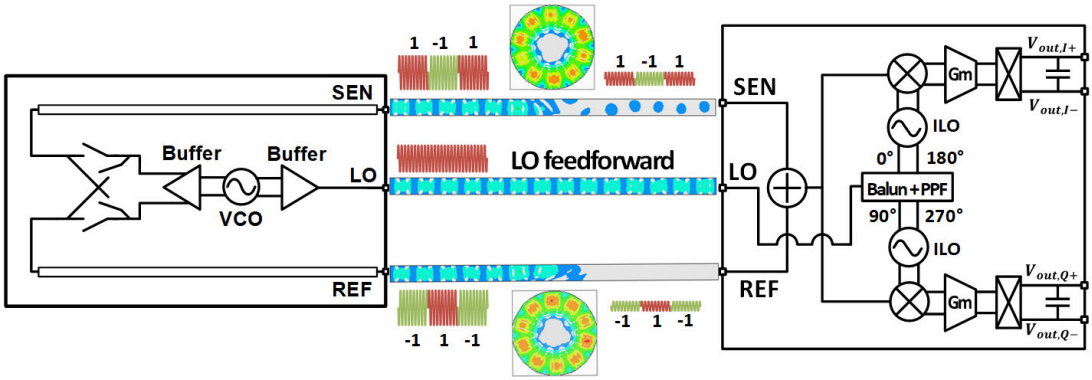

Fig. 8. Sensing system architecture.

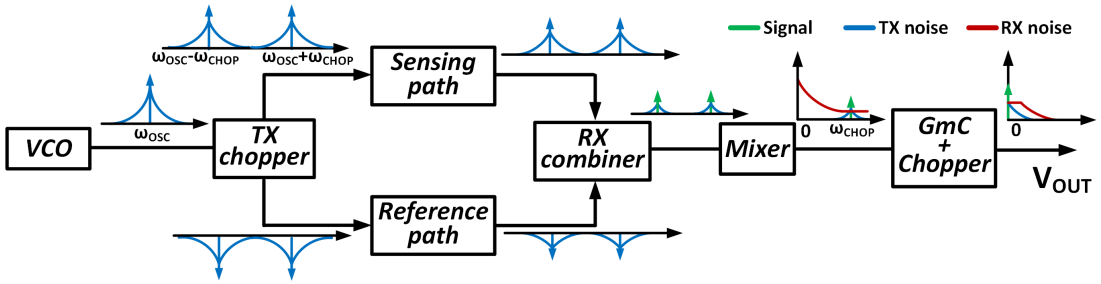

Fig. 9. Signal and noise propagation in critical nodes.

for simplicity. The TX chopper directly drives the sensing and the reference path with its differential outputs, respectively, and thus, the signals at the sensing and the reference paths always have opposite phase, forming the complementary BPSK signaling. The complementary signals are then attenuated by the sensors of the sensing path and the reference path by different amounts due to the permittivity difference of the MUT_{SEN} and MUT_{REF}. The attenuated complementary signals are then summed at the RX combiner. Due to the opposite phase of the complementary signaling, this addition is essentially the subtraction of the signals. The remaining part of this subtraction, which has a smaller amplitude, reflects the transmission difference of the sensing and the reference paths and, therefore, contains the information of $\Delta\epsilon_r$. The subtracted part is the common portion of the carriers from the two paths, which contains no information of $\Delta\epsilon_r$. Therefore, the true "signal" is 100% preserved from this subtraction. On the other hand, since the TX noise is dominated by the VCO phase noise, whose power is relative to the carrier power, a small signal carrier leads to a smaller TX noise power. In another words, the addition of the complementary signal improves the SNR by throwing away the TX noise associated with the portion of the carrier that contains no information of $\Delta\epsilon_r$. In the meanwhile, noises that are common to the two paths, such as the ambient temperature variation, are also eliminated by this subtracting process. The smaller amplitude of the remaining signal also mitigates the trade-off between noise and linearity for the RX circuitry. The resultant signal is then downconverted by the mixer to the frequency of $\omega_{\text{CHOP}} = 10$ MHz. The RX chopper inserted between the Gm stage and the integration capacitor finally demodulates the signal down to dc while upconverting all the low-frequency noise between the TX chopper and the RX chopper. At the same time, the TX injection locks the RX LO through a low-loss sub-THz LO feedforward path to suppress the TX's close-in phase noise in the downconversion process at the RX. The architectural combination of balanced sensing and reference path and the LO feedforward overcomes the drift and high close-in phase noise of a THz free running VCO, leading to a high sensing resolution. Sections III-B–III-D present the quantitative analysis of the signal and noise of the sensing system that guides the design of the TRX circuits.

B. Signal Flow

The system signal flow is illustrated in Fig. 10. $V_{\text{TX,SEN}} = V_{\text{TX,REF}} = \sqrt{P_{\text{TX}} Z_0}$ are the rms signal voltages at the output of the TX to the sensing paths and the reference paths, respectively. P_{TX} is the TX output power to the sensing path and the reference path, and $Z_0 = 50\ \Omega$. $V_{\text{RX,SEN}} = \sqrt{P_{\text{TX}} Z_0} S_{21,\text{SEN}}$ and $V_{\text{RX,REF}} = \sqrt{P_{\text{TX}} Z_0} S_{21,\text{REF}}$ are the signal voltages at the input of the RX to the sensing paths and the reference paths, respectively. $S_{21,\text{SEN}}$ and $S_{21,\text{REF}}$ are the transmission of the sensing path and reference path, respectively, and are both complex quantities. The RX sums these two signals before downconverting and amplification. Therefore, the magnitude of the RX output signal, $V_{\text{sig,out}}$, can be given by

$$\begin{aligned} V_{\text{sig,out}} &= \left|\sqrt{P_{\text{TX}} Z_0} S_{21,\text{SEN}} - \sqrt{P_{\text{TX}} Z_0} S_{21,\text{REF}}\right| \\ &\quad \cdot A_{V,\text{comb}} \cdot A_{V,\text{mixer}} \cdot A_{V,\text{GmC}} \\ &= \sqrt{P_{\text{TX}} Z_0} \left|S_{21,\ \text{SEN}} - S_{21,\text{REF}}\right| \\ &\quad \cdot A_{V,\text{comb}} \cdot A_{V,\text{mixer}} \cdot A_{V,\text{GmC}} \\ &= \sqrt{P_{\text{TX}} Z_0} |\Delta S_{21}| \cdot A_{V,\text{comb}} \cdot A_{V,\text{mixer}} \cdot A_{V,\text{GmC}} \\ &= \sqrt{P_{\text{TX}} Z_0} \text{Sen}_{\epsilon_r} \Delta\epsilon_r A_{V,\text{RX}} \end{aligned} \tag{3}$$

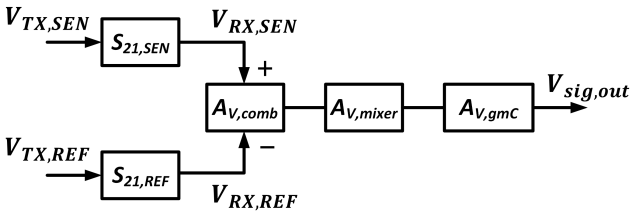

Fig. 10. System signal flow.

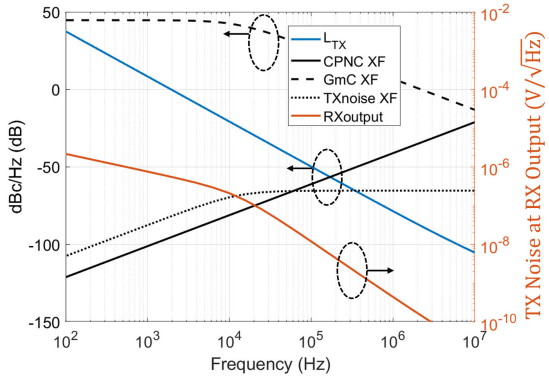

Fig. 11. L_{TX}, TX noise at the RX output and its transfer functions.

where $A_{V,\mathrm{comb}}$ is the voltage gain (loss) of the RX combiner, $A_{V,\mathrm{mixer}}$ is the conversion gain of the mixer, $A_{V,\mathrm{GmC}}$ is the dc gain of the Gm-C integrator, and $A_{V,\mathrm{RX}} = A_{V,\mathrm{comb}} \cdot A_{V,\mathrm{mixer}} \cdot A_{V,\mathrm{GmC}}$ is the total voltage gain of the RX. As can be seen, the output signal of the sensing system is proportional to the sensitivity of the sensor and the permittivity difference between the MUT on the sensing path and the reference path sensors.

C. Noise Analysis

Both TX and RX generate noise. The major source of the TX noise is the phase noise of the TX VCO, which is converted to amplitude noise in the direct conversion process of the RX mixer. The TX noise power density at the output of the TX can be modeled as $P_{\mathrm{TX}} Z_0 L_{\mathrm{TX}}(f)$, where $L_{\mathrm{TX}}(f)$ is the phase noise of TX signal in unit of dBc/Hz. As the TX noise is essentially the phase noise of signal carrier, it follows a similar process of the signal flow. At the output of the RX combiner, the TX noise power density is $P_{\mathrm{TX}} Z_0 L_{\mathrm{TX}}(f) \mathrm{Sen}_{\epsilon_r}^2 \Delta\epsilon_r^2 \cdot A_{V,\mathrm{comb}}^2$. At the output of the mixer, the TX noise power density becomes $P_{\mathrm{TX}} L_{\mathrm{TX}}(f) \mathrm{Sen}_{\epsilon_r}^2 \Delta\epsilon_r^2 \cdot A_{V,\mathrm{comb}}^2 A_{V,\mathrm{mixer}}^2 4|1 - e^{-j2\pi f t_d}|^2$. The factor 4 is due to the summing of the upper sideband and the lower sideband of the phase noise at output of direct conversion. $|1 - e^{-j2\pi f t_d}|$ is the coherent phase noise cancellation (CPNC) effect in the down conversion process, where t_d is the time delay difference between the RF and LO signals at the mixer, which is simulated to be 1.4 ns due to the high-quality factor of the resonator sensor [20]. With its high-pass feature, it suppresses the close-in phase noise. After passing the Gm-C integrator, the total TX noise at the RX output can then be given by

$$V_{n,\mathrm{TX}}^2 = \int_{f_L}^{f_H} P_{\mathrm{TX}} L_{\mathrm{TX}}(f) Z_0 (\mathrm{Sen}_\epsilon \Delta\epsilon)^2 A_{V,\mathrm{comb}}^2 A_{V,\mathrm{mixer}}^2 4 \left|1 - e^{-j2\pi f t_d}\right|^2 |H_{\mathrm{GmC}}(f)|^2 df \quad (4)$$

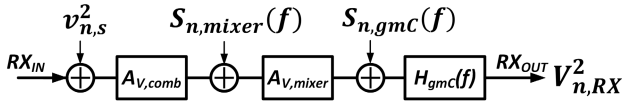

Fig. 12. RX noise model.

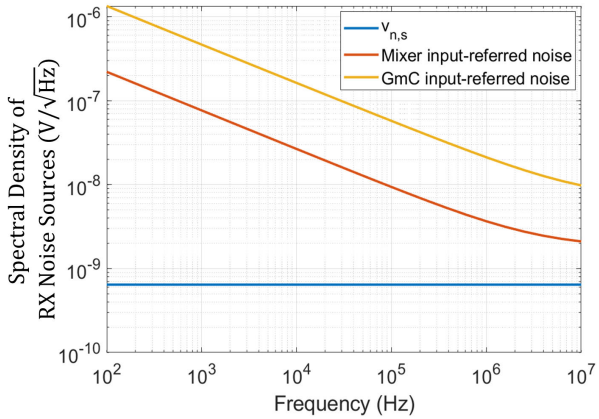

Fig. 13. Simulated RX noise.

where $H_{\mathrm{GmC}}(f)$ as in (13) is the transfer function of the time-windowed integrator and is derived in Section IV. The transfer function of the CPNC process and the overall RX on the TX noise, and the TX noise power spectral density at the RX output are plotted in Fig. 11. The integration limit f_L and f_H in (4) and in all the following noise analysis should be chosen carefully, to accurately quantify the total noise voltage sampled at the RX output. The lower bound of the integration f_L is chosen to be 100 Hz, which is much lower than the integration clock cycles of 50 kHz, and the upper bound of the integration f_H is chosen to be 100 MHz, which is much higher than the GmC corner frequency of 20 kHz.

Fig. 12 shows the noise model of the RX. $v_{n,s}^2 = 2kTZ_0$ is the kT noise of the 50-Ω source impedance of the two-input RX. The input-referred noise power density of the mixer can be modeled as a combination of the mixer's thermal noise and flicker noise

$$S_{n,\mathrm{mixer}}(f) = v_{n,\mathrm{mixer}}^2 + \frac{k'_{\mathrm{mixer}}}{f} \quad (5)$$

where $v_{n,\mathrm{mixer}}^2$ is the power density of mixer's thermal noise and k'_{mixer} is the mixer's flicker noise factor. Similarly, the noise power density of the Gm-C integrator is modeled as follows:

$$S_{n,\mathrm{GmC}}(f) = v_{n,\mathrm{GmC}}^2 + \frac{k'_{\mathrm{GmC}}}{f}. \quad (6)$$

The simulated RX noise sources are plotted in Fig. 13. As discussed in Section IV-B, the mixer is designed to have lower input referred noise than the Gm-C circuit to lower the overall noise figure (NF) of the RX. Also, the noise from the mixer and the Gm-C circuit dominates the kT noise $v_{n,s}$. Therefore, $v_{n,s}$ is neglected in the following analysis for simplicity. The total RX noise at the output is then given by

$$V_{n,\mathrm{RX}}^2 = \int_{f_L}^{f_H} \left[S_{n,\mathrm{mixer}} A_{V,\mathrm{mixer}}^2 |H_{\mathrm{GmC}}(f)|^2 + S_{n,\mathrm{GmC}} |H_{\mathrm{GmC}}(f)|^2\right] df. \quad (7)$$

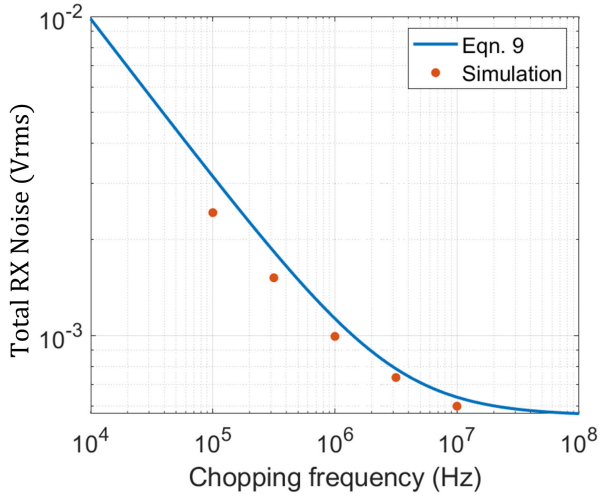

Fig. 14. Total RX noise at the RX output for different chopping frequencies.

Plugging (5) and (6) into (7), we get

$$V_{n,\mathrm{RX}}^2 = \int_{f_L}^{f_H} \left[\left(v_{n,\mathrm{mixer}}^2 + \frac{k'_{\mathrm{mixer}}}{f} \right) A_{V,\mathrm{mixer}}^2 |H_{\mathrm{GmC}}(f)|^2 + \left(v_{n,\mathrm{GmC}}^2 + \frac{k'_{\mathrm{GmC}}}{f} \right) |H_{\mathrm{GmC}}(f)|^2 \right] df. \quad (8)$$

With chopping, the flicker noise component at f_{chop} is downconverted to dc. With the detailed derivation shown in Appendix A, the total RX noise can be approximated as follows:

$$V_{n,\mathrm{RX}}^2 \approx \int_{f_L}^{f_H} \left[\left(v_{n,\mathrm{mixer}}^2 + \frac{8k'_{\mathrm{mixer}}}{\pi^2 f_{\mathrm{chop}}} \right) A_{V,\mathrm{mixer}}^2 |H_{\mathrm{GmC}}(f)|^2 + \left(v_{n,\mathrm{GmC}}^2 + \frac{8k'_{\mathrm{GmC}}}{\pi^2 f_{\mathrm{chop}}} \right) |H_{\mathrm{GmC}}(f)|^2 \right] df. \quad (9)$$

It can be observed that, as the mixer precedes the Gm-C integrator, its noise is amplified by the mixer gain and, therefore, is more critical. The input-referred noise or, equivalently, the NF of the mixer and should be minimized by design. Equation (9) also shows that higher chopping rate results in lower total RX noise due to the lowered contribution from the flicker noise of the mixer and the Gm-C integrator. Qualitatively, this is because the flicker noise is modulated to frequencies further away from dc, where the signal resides at the output of the RX. This is verified by simulation, as shown in Fig. 14, where total RX noise reduces, as chopping rate f_{chop} increases. It can also be observed from Fig. 14 that this noise reduction effect is less significant for higher chopping rate, because the thermal noise starts to dominate, which cannot be suppressed by chopping, as shown in (9). However, a higher chopping rate requires the operational transconductance amplifier (OTA) to have higher bandwidth. Eventually, a balanced chopping rate of 10 MHz is chosen. Fig. 15 shows the simulated noise spectral densities of the various noise types shown at the output of the system. The chopping suppresses the RX noise that is generated between the choppers in the TX and the RX, and the CPNC suppress the TX noise under the RX noise. The circuit simulation results further validate the foregoing theoretical noise analysis in Section III-D of SNR analysis.

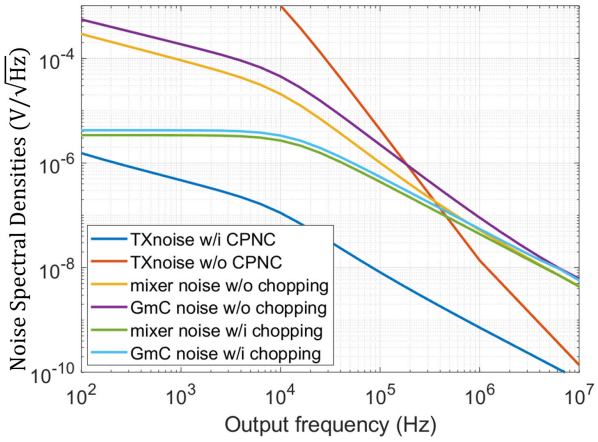

Fig. 15. Noise spectral densities of different noises at the RX output.

D. SNR and Resolution

The SNR of the system can be expressed as follows:

$$\mathrm{SNR} = \frac{V_{\mathrm{sig,out}}^2}{V_{n,\mathrm{RX}}^2 + V_{n,\mathrm{TX}}^2}. \quad (10)$$

Setting SNR = 1, at the detection limit, the total noise equals the signal at the RX output

$$V_{n,\mathrm{RX}}^2 + V_{n,\mathrm{TX}}^2 = P_{\mathrm{TX}} Z_0 \mathrm{Sen}_{\epsilon_r}^2 \delta\epsilon_r^2 A_{V,\mathrm{RX}}^2 P \quad (11)$$

where $\delta\epsilon_r$ is the minimum detectable permittivity difference or the sensing resolution, and $V_{n,\mathrm{TX}}^2$ and $V_{n,\mathrm{RX}}^2$ are expressed by (4) and (9), respectively. Note that $\delta\epsilon_r$ also exists in $V_{n,\mathrm{TX}}^2$, again showing the TX noise dependence on the signal strength. Factoring out $\delta\epsilon_r$ in both sides of the equation and squaring root both sides, $\delta\epsilon_r$ can be expressed as (12) The signal, noise, and the resolution versus the measurement integration time are shown in Fig. 16. The signal and, therefore, the TX noise increase by 20 dB/dec, as the Gm-C integrator integrates for longer time. The increase of the signal and the noises saturates at around 10 μs due to the finite output resistant of the OTA, as shown in Fig. 26(b). It can be observed from Fig. 26(a) that the bandwidth of the integrator is inversely proportional to the integration time, while its gain $A_{V,\mathrm{GmC}}$ is proportional to the integration time. Since the RX noise at the system output is mostly white, its total noise power is proportional to $\sqrt{BW}$ (10 dB/dec) and $A_{V,\mathrm{Gm}}$ (20 dB/dec). Hence, as a typical behavior of an integrator, the combination of the higher gain but smaller noise bandwidth due to the longer integration time results in the increase rate of the RX noise of 10 dB/dec before it saturates. Because the RX noise dominates over the TX noise, the signal increases 10 dB/dec faster than the total noise, and therefore, the resolution improves with the integration time with a −10-dB/dec slope before the integration saturates. The signal, noise, and the resolution versus the TX output power are shown in Fig. 17. With increased TX output power, signal and TX noise increase, while the RX noise remains independent on TX output power, as expected. The SNR and, therefore, resolution improve, because RX noise is dominating. The systematic analysis above guides the design decisions and the power spending strategies in the TX and RX design process, as shown in Section IV.

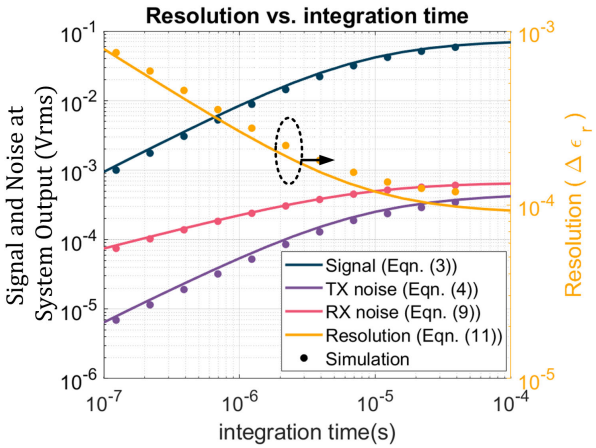

Fig. 16. Theoretical and simulated signal, TX noise, and RX noise voltage at the system output and resolution versus integration time.

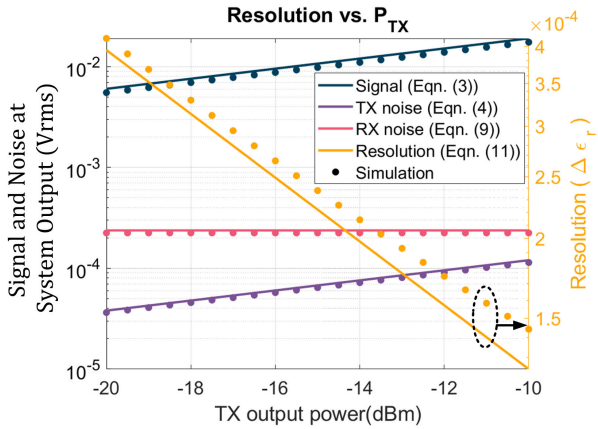

Fig. 17. Theoretical and simulated signal, TX noise, and RX noise voltage at the system output and resolution versus TX output power.

IV. Circuit Implementation

A. TX

The block diagram of the TX is shown in Fig. 8, and the schematic and the core passive layout of the TX are shown in Fig. 18. The TX generates sub-THz excitation for the sensors and provides injection LO to the RX to suppress the phase noise associated with the excitation signals in the sensing and reference paths. For this prototype, the TX should meet three requirements: the LO output power should be large enough to injection-lock the RX; based on Fig. 7(b), the sensing and the reference path power should be large enough to achieve a permittivity sensing resolution to the order of 10^{-4}; the TX's output frequency should have a tuning range of 8 GHz to cover the resonant frequency shift caused by the common dielectric materials. Based on the simulation results, to injection-lock the RX injection-locked oscillators (ILOs) with a frequency range of 8 GHz, the minimum required input power at the RX's LO port is -15 dBm. Considering the 4-dB insertion loss of the LO feedforward path from the sensor structure's simulation, the LO buffer needs an output power of -8 dBm to have some safe margin. Designed as a class-A power amplifier, the load line simulation of the LO buffer determines the device size of the pseudo-differential pair to be 6.7 μm, resulting in a dc power consumption of 9 mW for the LO buffer. A load–pull simulation determines that the optimum load impedance of the pseudo-differential pair for maximum output power is $Z_{\text{opt}} = 130 + j205\ \Omega$. A transformer-based balun T_{LO} converts $Z_0 = 50\ \Omega$ to Z_{opt} with a loss of 2 dB. The RF buffer delivers differential signals to the sensing and reference paths through the TX chopper. The buffer's device size has a direct impact on the output power level and, therefore, the system SNR. However, larger device also loads the VCO tank, resulting a small swing at the input of the buffer if the VCO devices are not widened correspondingly [21]. To limit the overall power consumption of the sensing system, the device is chosen to be 6.7-μm wide, identical to the LO buffer, also to maintain layout symmetry. Therefore, the RF buffer has the same Z_{opt} as the LO buffer. Before designing the RF buffer's impedance matching transformer T_{RF}, the TX chopper is designed first, so that its parasitics can be absorbed into the impedance matching. The device size of the chopper is chosen to be 12 μm to have the minimum power loss of 4.4 dB. This is also the device size ensuing the best on–off ratio for each switch. The opposite-phase square-wave chopping signals are applied to the gates of the chopper switches to modulate the signals on the sensing and reference paths into BPSK signals. As can be seen in Figs. 18 and 21, the signals with equal amplitude but opposite phase diverge at the output of the chopper to the sensing and reference path outputs, respectively, through the identical 431-μm 50-Ω CPWs, which have a loss of 1.5 dB. The transformer of the signal buffer is then designed to match the input impedance of the chopper to Z_{opt}.

For the generation of sub-THz signal in CMOS technology, harmonic oscillator and fundamental oscillator with multiplier are the common methods, due to the fact that the operation frequency is close to f_{max} of the device [22], [23]. By contrast, fundamental oscillator is more efficient, without the need of the extraction of the weaker harmonics, yet it is also more challenging to design due to the higher loss of the passives and lower activity of the CMOS device at this frequency. In this work, to minimize the power consumption, a fundamental VCO is adopted to generate the 160-GHz signal for the sensing system. To achieve a tuning range of 8 GHz, a combination of the MOS varactors pair and a single-bit discrete capacitor are used. The VCO device size is determined to be 5 μm to achieve an LO output power of -8 dBm, as shown in Fig. 19, with the loading of the varactors and the discrete cap. The cross-coupled devices contribute 8-fF parasitic capacitance to

$$\delta\epsilon_r = \sqrt{\frac{\int_{f_L}^{f_H}\left(v_{n,\text{mixer}}^2 + \frac{8k'_{\text{mixer}}}{\pi^2 f_{\text{chop}}}\right)A_{V,\text{mixer}}^2|H_{\text{GmC}}(f)|^2 + \left(v_{n,\text{GmC}}^2 + \frac{8k'_{\text{GmC}}}{\pi^2 f_{\text{chop}}}\right)|H_{\text{GmC}}(f)|^2 df}{P_{\text{TX}}Z_0\text{Sen}_{\epsilon_r}^2 A_{V,\text{RX}}^2 - \int_{f_L}^{f_H} P_{\text{TX}}L_{\text{TX}}(f)Z_0\text{Sen}_{\epsilon}^2 A_{V,\text{comb}}^2 A_{V,\text{mixer}}^2 4|1 - e^{-j2\pi f t_d}|^2|H_{\text{GmC}}(f)|^2 df}} \tag{12}$$

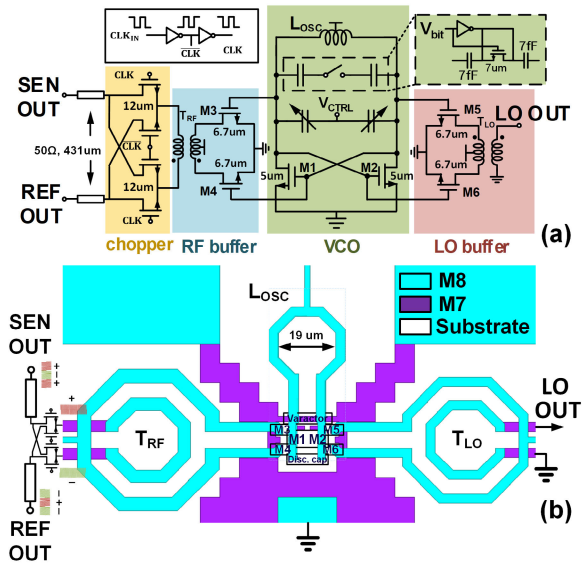

Fig. 18. TX circuit. (a) TX schematic. (b) Core layout.

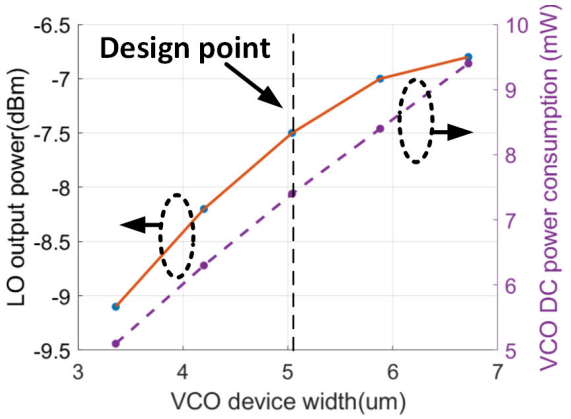

Fig. 19. VCO device sizing and LO output power and dc power consumption.

the VCO's resonant tank and consume 8 mW of dc power. At 160 GHz, the quality factor of the varactor is significantly lower than those in the GHz range. To achieve an 8-GHz tuning range, a varactor size of 0.32 μm^2 is chosen, whose quality factor varies from 28 to 5.5. To minimize the ground loss of the core area layout, the top two layers of thick metal M8 and M7 are used as ground in the core area, as shown in Fig. 18(b). By the careful design and layout, the VCO generates a differential voltage amplitude >800 mV at its drain nodes, which directly drives the gates of the LO and RF buffer devices.

The simulated performance of the TX is shown in Fig. 20. The LO buffer delivers the output power of −8 to −3 dBm to the LO output port within the TX frequency tuning range. Also, the output power of the sensing and reference paths is from −11.5 to −16.5 dBm within the TX frequency sweep range. The output power of the sensing and reference port is lower than the LO port, because the signal buffer drives two 50-Ω paths at the same time, on top of the additional loss of the chopper and the routing CPWs. The output power difference of the sensing and reference paths is due to the layout mismatch of the TX. This mismatch, along with the sensor's fabrication

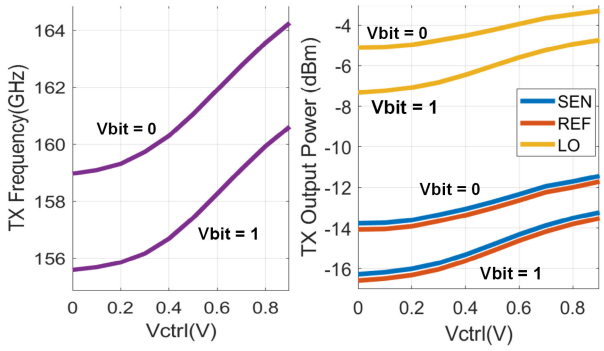

Fig. 20. TX frequency tuning range and output power.

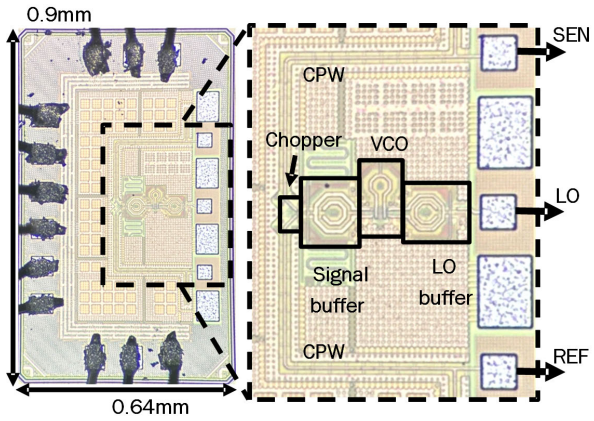

Fig. 21. Chip micrograph of the TX and the zoomed-in core area.

mismatch, can be calibrated out in the measurement process. The simulated phase noise of the TX is shown in Fig. 10. The TX chip is fabricated in 28-nm bulk CMOS technology, and the chip photograph is shown in Fig. 21.

B. RX

The combiner's schematic and simulated performance are shown in Fig. 22, and its layout can be seen from the RX chip photograph in Fig. 27. It is made of five sections of CPW, and it combines the signal from the sensing and referencing paths. The combined signal is then split and delivered to the input of the mixers of the I and Q paths. The loss of the combiner is 5.2 dB.

At sub-THz, the power efficiency of the low-noise amplifier in terms of its effectiveness of lowering the NF of the entire RX is much lower than the GHz counterparts. Therefore, the RX adopted mixer-first topology. The design goal for the mixer is to have a reasonable NF and gain within a limited power budget to dictate an optimum noise performance of the overall RX. The mixer's schematic is shown in Fig. 23. A single-ended Gilbert cell serves as a natural balun to avoid the loss of the passive balun at sub-THz frequencies. The Gm device is chosen to be 20-μm wide to have a transconductance of 22 mS; 3.3 out of 3.5-mA dc current from the Gm device is bled to a PMOS current helper to relieve the current steering load of the switching devices. Less steering current allows the switching device to spend less time in transition, resulting in a better gain and noise performance. Less dc current also allows using larger load resistance and helps reduced the flicker noise

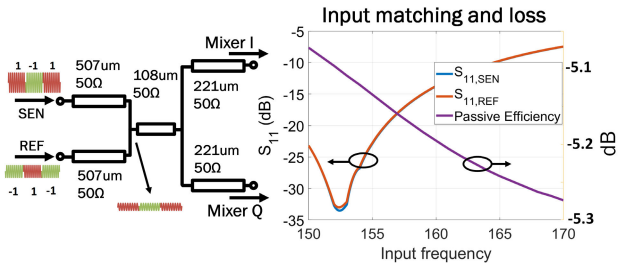

Fig. 22. Combiner schematic and simulated performance.

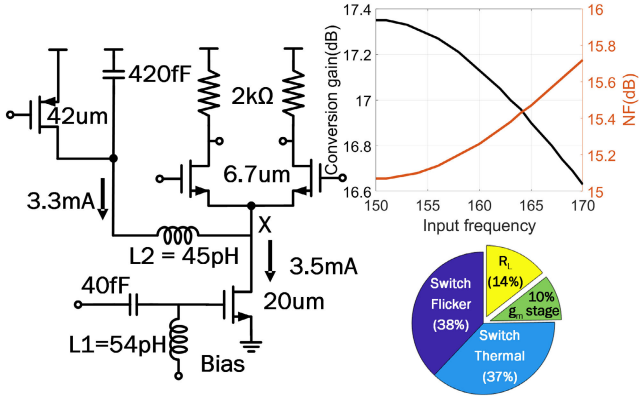

Fig. 23. Mixer schematic, performance, and noise contribution.

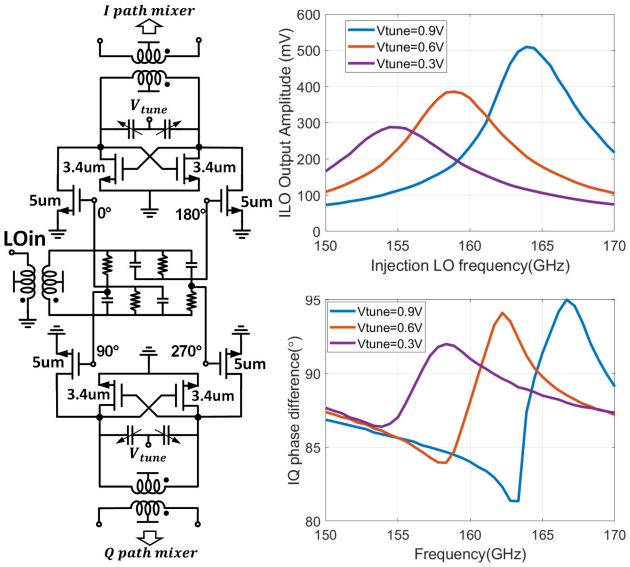

Fig. 24. ILO schematic, output amplitude, and I/Q phase difference.

of the switch devices, which further boost the gain and noise performance of the mixer.

The parasitic capacitance at node X steals away signal current from the Gm device and increases the switching devices noise contribution to the output by lowering the impedance at the node. The inductor $L2$ of 45 pH and $Q = 9$ in the current bleeding path is used to resonate out the parasitic capacitance. The voltage gain of the mixer is around 17 dB, and the NF is about 15.4 dB. The switch devices contribute most of the noise due to the relative low impedance at node X and the moderate differential LO voltage amplitude about 400 mV at 160 GHz. The ILO's schematic is shown in Fig. 24. The ILO needs to have 8-GHz lock range to cover the measurement range and high output voltage swing at the mixer's LO port to maximize the mixer gain. To provide quadrature LO for the mixers of the I/Q path, the design of an RC poly-phase filter feeding two standalone ILO is adopted to avoid using the lossy quadrature coupler for quadrature oscillation generation that is commonly used in low-frequency quadrature ILOs [24]. The resulting phase mismatch of the I/Q paths can be calibrated out in the measurement as a static process. An input balun converts the incoming TX LO signal to differential signal that drives the RC poly-phase filter to generate the two pairs of quadrature signals. From simulation, to have a 15-dB conversion gain, the mixer requires a 400-mV amplitude differential voltage at the gate of its LO devices. To achieve a reasonable lock range with this output amplitude requirement, two methods are adopted. First, the injection devices are larger than the oscillator device to have a strong enough injection to achieve a larger lock range. A pair of varactors are used to further increase the overall lock range by tuning the self-oscillation frequency of the core oscillator. From simulation, with a -12-dBm injection power delivered at the RX's LO port, the lock range with larger than 400-mV LO amplitude is 12 GHz to have a safe margin for process variation, as shown in Fig. 24.

The Gm-C integrator is implemented with a folded telescopic OTA as the Gm stage and a 52-pF on-chip integration capacitor, as shown in Fig. 25(a). The OTA is designed to have low input-referred noise and high output resistance to achieve a high SNR. A chopper is inserted between the OTA and the capacitor to suppress the flicker noise of the OTA and the mixer, as shown in Fig. 25(b). The hold and reset switches control the integration period, as shown in Fig. 25(c). Comparing with [13], the separation of the chopping and hold switch allows a longer integration time than the chopping period, resulting in a higher SNR. The dc offset and low-frequency noise are removed by the multiple chopping periods within one integration cycle. With the detailed derivation shown in Appendix B, the transfer function of the Gm-C integrator with the integration time of $t = t_{\text{int}}$ is expressed as follows:

$$H_{\text{GmC}}(s) = \frac{\text{GmR}_{\text{out}}(1 - e^{-st_{\text{int}}})}{1 - e^{-st_{\text{int}}} + R_{\text{out}}sC_{\text{int}}} \tag{13}$$

which is plotted in Fig. 26(b) for different $t = t_{\text{int}}$. A longer integration time results in a larger dc gain and smaller equivalent noise bandwidth (ENBW) and, hence, higher SNR. As can be seen, however, comparing with an ideal Gm-C integrator in Fig. 26(a), the increase of the gain and decrease of the bandwidth start to saturate, as t_{int} increases above 10 μs. This saturation behavior is also manifested in the saturation of the resolution improvement with longer integration time in Fig. 16.

This deviation from the ideal Gm-C's behavior is caused by the finite output resistance $R_{\text{out}} = 150\ k\Omega$ of the OTA, and the maximum integration time is constrained by the output resistance of the OTA. With $R_{\text{out}} = 150\ k\Omega$, the maximum integration time is around 14 μs, which results in a dc gain of 50 dB and an ENBW of 20 kHz.

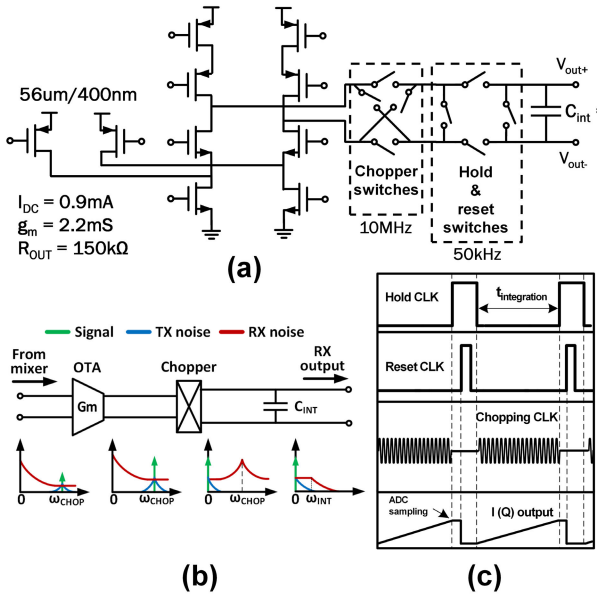

Fig. 25. Gm-C integrator. (a) Circuit schematic. (b) Illustration of signal and noise processing. (c) Signal processing timing.

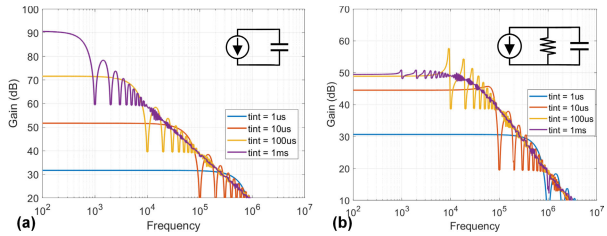

Fig. 26. Transfer functions of (a) ideal Gm-C integrator and (b) practical Gm-C integrator with finite output resistance.

V. Measurements

The fabricated sensor structure is packaged with the TX and RX chips with bonding wires on PCB board, as shown in Fig. 28. Careful measures to minimize the length of the bonding wires include minimizing the gap between the chip and the sensor interposer and making the top surfaces of the interposer and the chip have the same height. Using wedge bonding also results in shorter wire length comparing with ball bonding. The chip–interposer interface is modeled and electromagnetic field (EM) simulated in high frequency simulation software (HFSS), and the extracted inductance of the bonding wire is around 60 pH. The EM model of the interface is included in the simulations of the TX output matching network and RX input matching network, respectively, to incorporate the bonding wire effect.

The permittivity measurement setup is shown in Fig. 29. Rogers microwave circuit board substrates are placed on top of the sensors of the sensing and reference path as MUT samples. The samples are of the same dimensions as in the simulations in Section II. A single Teensy Arduino microcontrol unit (MCU) is sufficient to provide all the clocking and control signals for the TX and RX. The TX's output frequency is controlled by V_{cont}, which is swept in each sample measurement. The 10-MHz chopping clock is provided by the MCU to both the TX and RX. The hold and the reset

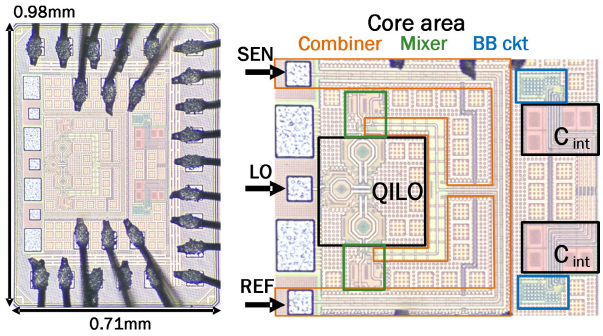

Fig. 27. Chip micrograph of the RX and the zoomed-in core area.

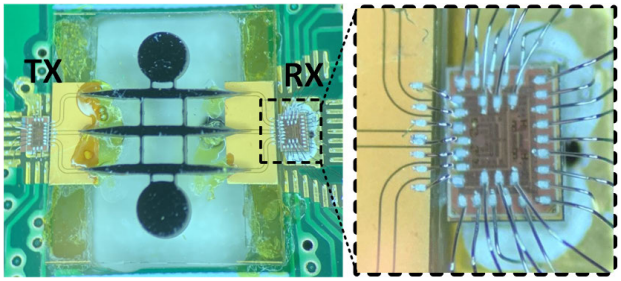

Fig. 28. Sensing system packaging.

clock of the RX's integrator are also provided by the MCU to control the integration time. The hold and reset clocks are set to have a frequency of 50 kHz. With 70% duty cycle, it gives an integration time of 14 μs. The output waveform of I path $V_{\text{out},I}$ is observed by oscilloscope, as shown in Fig. 30(a). The output waveform (yellow curve) of four cycles of integration is shown together with the hold clock (green curve). The RX outputs $V_{\text{out},I}$ and $V_{\text{out},Q}$ are sampled by the data acquisition module NI DAQ9174, whose sampling is triggered by the rising edge of the hold clock of the RX to make sure the output voltages are sampled at the end of each integration cycle. $V_{\text{out},I}$ and $V_{\text{out},Q}$ are then used to construct the ΔS_{21} of different dielectric samples placed on top of the sensors of the sensing and reference paths, as shown in Fig. 30(b). In Fig. 30(b), V_{cont} is swept from 380 to 880 mV to obtain the transmission difference waveform of the sensing and reference paths when different MUT samples are placed on the sensors. Fig. 31 shows the system outputs when the Rogers 5870 samples of different thicknesses are placed on the sensing and reference paths. Simulation results from Fig. 7(b) are also plotted in the same figure against the measurement results. These measurements emulate the permittivity measurement process of an unknown MUT sample by comparing its transmission difference with the simulation result when the reference MUT on the reference path is the known MUT Rogers 5870 with the same thickness.

The system output noise is measured with no samples on either sensor disks, as shown in Fig. 32. Its noise spectral density shows that low-frequency noise is suppressed by the chopping. With chopping, the rms value of the system output noise floor is measured to be 0.45 mV. The SNR of the

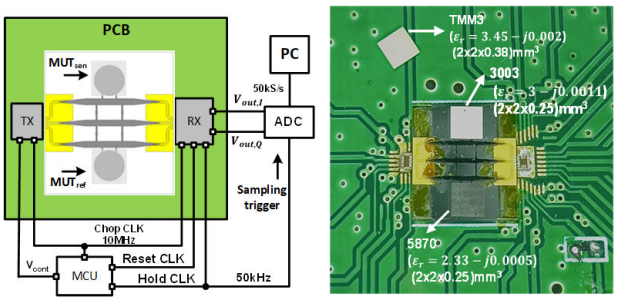

Fig. 29. Permittivity measurement setup.

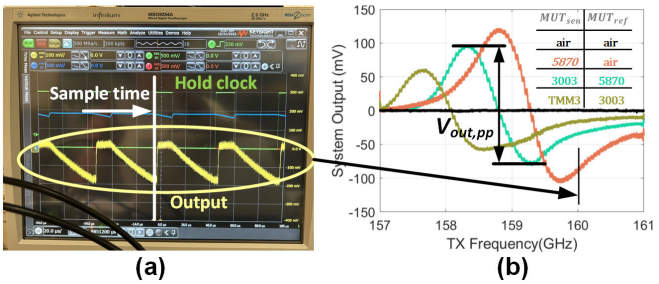

Fig. 30. Sensing system output observed in (a) oscilloscope and (b) PC through analog-to-digital converter (ADC).

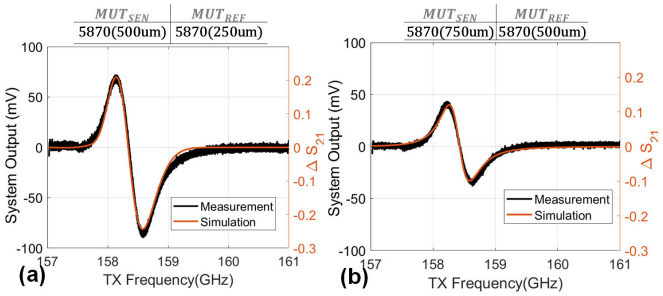

Fig. 31. Sensing system output with different thicknesses of Rogers 5870 samples placed on the sensors. (a) 500-μm-thick 5870 versus 250-μm-thick 5870. (b) 750-μm-thick 5870 versus 500-μm-thick 5870.

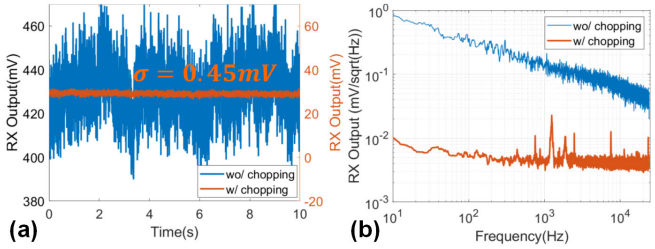

Fig. 32. System output noise. (a) Time-domain output noise. (b) Spectral density of (a).

measurements is calculated by

$$\mathrm{SNR} = \frac{V_{\mathrm{out,pp}}^2}{v_{n,\mathrm{out}}^2} \tag{14}$$

where $V_{\mathrm{out,pp}}$ is the peak–peak voltage of the system output due to permittivity difference between the sensing and the reference path, and $v_{n,\mathrm{out}}$ is the rms voltage of the system output noise floor.

The relative permittivity sensing resolution of the sensing system is calculated by dividing the normalized permittivity difference of the measured samples that causes the $V_{\mathrm{out,pp}}$ by the square root of the resulting SNR

$$\delta_{\epsilon_r} = \frac{\widehat{\Delta\epsilon_r}}{\sqrt{\mathrm{SNR}}}. \tag{15}$$

The normalized permittivity difference is defined as follows:

$$\widehat{\Delta\epsilon_r} = \frac{|\Delta\epsilon_r|}{|\epsilon_{r,\mathrm{SEN}} + \epsilon_{r,\mathrm{REF}}|/2} = \frac{|\epsilon_{r,\mathrm{SEN}} - \epsilon_{r,\mathrm{REF}}|}{|\epsilon_{r,\mathrm{SEN}} + \epsilon_{r,\mathrm{REF}}|/2}. \tag{16}$$

When $\Delta\epsilon_r$ is purely real, namely, when the sensing material and the reference material have only real permittivity difference, the real permittivity sensing resolution can be calculated by (15), similarly for the calculation of the imaginary permittivity sensing resolution. Also, when $\Delta\epsilon_r$ is a complex number, δ_{ϵ_r} represents the complex sensing resolution. Table I summarizes the measurement results. Note that the MUTs in the measurement all have relatively small ϵ_r'', and hence, the calculated resolutions mostly represent the real permittivity sensing resolution of the sensing system. The sensing resolution of 0.05% is found by a 14% permittivity difference between the Rogers 3003 and Rogers TMM3 samples divided by the resulting $\sqrt{\mathrm{SNR}}$ of 262.

Table II compares this work with the prior art. To have a fair and more straightforward comparison, a figure of merit (FoM) for integrated permittivity sensors is defined as follows:

$$\mathrm{FoM} = -10\log\left(\delta_{\epsilon_r}^2 P_{\mathrm{dc}} \tau_{\mathrm{int}}\right) \tag{17}$$

where δ_{ϵ_r} is the permittivity sensing resolution, P_{dc} is the dc power consumption, and τ_{int} is the integration time. Thus, this work also demonstrates the highest FoM factor by achieving the best resolution with low-power consumption and short measurement time.

TABLE I
MEASUREMENT RESULTS SUMMARY

Case	1	2	3	4	5
MUT_{SEN}	5870	3003	TMM3	5870 (500um)	5870 (750um)
MUT_{REF}	Air	5870	3003	5870 (250um)	5870 (500um)
$\epsilon_{r,SEN}$	2.33-j0.0005	3-j0.0011	3.45-j0.002	*2.77-j0.0007	*2.95-j0.0008
$\epsilon_{r,REF}$	1	2.33-j0.0005	3-j0.0011	2.33-j0.0005	*2.77-j0.0007
$\widehat{\Delta\epsilon_r}\%$	79.9	25.1	14.0	17.3	6.3
$V_{PP}(mV)$	223.4	117.7	118.1	155.5	87.6
$v_{n,out}(mV)$	0.45	0.45	0.45	0.45	0.45
SNR($\times 10^3$)	256	156	68.9	119	37.9
Resol.%	0.16	0.064	0.053	0.05	0.032

* Equivalent permittivity for sample with 250-um thickness;

VI. CONCLUSION

This article presents a high-resolution-integrated permittivity sensor at 160 GHz in 28-nm CMOS. It advances the state-of-the-art complex permittivity sensing resolution by adopting a high-sensitivity silicon WGM resonator sensor and a novel architectural combination of complementary BPSK chopping and CPNC with LO feedforward to the RX. The

TABLE II
COMPARISON WITH THE STATE-OF-THE-ART-INTEGRATED PERMITTIVITY SENSOR

	JSSC'16 [10]	JSSC'20 [13]	TMTT'18 [25]	TMTT'19 [7]	CICC'21 [26]	JERM'18 [8]	This Work
Technology	65nm CMOS	180nm CMOS	40nm CMOS	65nm CMOS	45nm RFSOI	250nm BiCMOS	28nm CMOS
Frequency(GHz)	6.5/11/17.5/30	1.8/2.2	0.1-10	3-10	$\lambda = 1300nm$	30	154-160
Resolution(%)	0.8	0.3	3	0.2	0.08	3.7	0.05
Integration time(us)	10	20.48	1000	150	10000	1000	14
Complex sensing	No	No	Yes	Yes	No	No	Yes
Integrated LO	Yes	Yes	No	Yes	No	No	Yes
Power consump.(mW)	65	77.7	24	64	128	60	54
FoM	103.8	108.4	76.7	104.2	90.9	70.8	127.2

sensing system achieves a permittivity sensing resolution of 0.05% $\Delta\epsilon_r$ as well as the highest FoM within 14 μs of integration time.

APPENDIX A

The following derivation verifies the flicker noise contribution at the RX output near dc (within ENBW, that is $f <$ ENBW) after the chopper by modeling the chopping process as frequency-domain convolution with the harmonics of the square wave:

$$v^2_{1/f,\text{out}}(f) = v^2_{1/f,\text{in}}(f) * H^2_{\text{chop}}(f)$$
$$v^2_{1/f,\text{out}}(f) = \frac{k}{f} * 2\sum_{n=1}^{\infty}\left[\frac{2}{(2n-1)\pi}\right]^2 \delta[f + (2n-1)f_{\text{chop}}]$$

$$v^2_{1/f,\text{out}}(f) = \int_{-\infty}^{\infty}\frac{k}{\nu}\cdot 2\sum_{n=1}^{\infty}\left[\frac{2}{(2n-1)\pi}\right]^2 \cdot\delta\left[\nu - \left(f + (2n-1)f_{\text{chop}}\right)\right]df. \quad (18)$$

By sifting property of the Dirac delta function, we get

$$v^2_{1/f,\text{out}}(f) = 2\sum_{n=1}^{\infty}\left[\frac{2}{(2n-1)\pi}\right]^2 \frac{k}{f + (2n-1)f_{\text{chop}}}$$

$$v^2_{1/f,\text{out}}(f) = 2\left(\frac{2}{\pi}\right)^2\frac{k}{f+f_{\text{chop}}} + 2\left(\frac{2}{3\pi}\right)^2\frac{k}{f+3f_{\text{chop}}} + 2\left(\frac{2}{5\pi}\right)^2\frac{k}{f+5f_{\text{chop}}} + \cdots \quad (19)$$

when $f \ll f_{\text{chop}}$, which is the case when $f <$ 20 kHz after chopping

$$v^2_{1/f,\text{out}}(f) = 2\left(\frac{2}{\pi}\right)^2\frac{k}{f_{\text{chop}}} + 2\left(\frac{2}{3\pi}\right)^2\frac{k}{3f_{\text{chop}}} + 2\left(\frac{2}{5\pi}\right)^2\frac{k}{5f_{\text{chop}}} + \cdots \approx = 2\left(\frac{2}{\pi}\right)^2\frac{k}{f_{\text{chop}}} = \frac{8}{\pi^2}\frac{k}{f_{\text{chop}}}. \quad (20)$$

APPENDIX B

This appendix section shows the derivation of the transfer function of the windowed Gm-C integrator, whose equivalent circuit models are shown in Figs. 33 and 34. The output voltage across the integration capacitor after the integration finishes($t > t_{\text{int}}$) can be expressed as follows:

$$V_{\text{out}}(t) = \frac{1}{C_{\text{int}}}\int_0^{t_{\text{int}}} G_m \cdot V_{\text{in}}(\tau) - \frac{V_{\text{out}}(\tau)}{R_{\text{out}}}d\tau. \quad (21)$$

In order to derive the frequency-domain transfer function, some manipulation is needed before performing the Laplace transformation

$$V_{\text{out}}(t) + \frac{1}{C_{\text{int}}}\int_0^{t_{\text{int}}}\frac{V_{\text{out}}(\tau)}{R_{\text{out}}}d\tau = \frac{1}{C_{\text{int}}}\int_0^{t_{\text{int}}} G_m \cdot V_{\text{in}}(\tau)d\tau \quad (22)$$

$$V_{\text{out}}(t) + \frac{1}{C_{\text{int}}}\left[\int_0^{t}\frac{V_{\text{out}}(\tau)}{R_{\text{out}}}d\tau + \int_t^{t_{\text{int}}}\frac{V_{\text{out}}(\tau)}{R_{\text{out}}}d\tau\right] = \frac{1}{C_{\text{int}}}\left[\int_0^{t_{\text{int}}} G_m \cdot V_{\text{in}}(\tau)d\tau + \int_t^{t_{\text{int}}} G_m \cdot V_{\text{in}}(\tau)d\tau\right] \quad (23)$$

$$V_{\text{out}}(t) + \frac{1}{C_{\text{int}}R_{\text{out}}}\left[\int_0^{t} V_{\text{out}}(\tau)d\tau - \int_{t_{\text{int}}}^{t} V_{\text{out}}(\tau)d\tau\right] = \frac{G_m}{C_{\text{int}}}\left[\int_0^{t_{\text{int}}} V_{\text{in}}(\tau)d\tau - \int_{t_{\text{int}}}^{t} V_{\text{in}}(\tau)d\tau\right]. \quad (24)$$

Using the convolution property of Heaviside function $x(t) * u(t) = \int_0^t x(\tau)d\tau$, the above equation can be written as follows:

$$V_{\text{out}}(t) + \frac{1}{C_{\text{int}}R_{\text{out}}}[V_{\text{out}}(t) * u(t) - V_{\text{out}}(t) * u(t - t_{\text{int}})] = \frac{G_m}{C_{\text{int}}}[V_{\text{in}}(t) * u(t) - V_{\text{in}}(t) * u(t - t_{\text{int}})] \quad (25)$$

$$V_{\text{out}}(t) + \frac{V_{\text{out}}(t)}{C_{\text{int}}R_{\text{out}}} * [u(t) - u(t - t_{\text{int}})] = \frac{G_m}{C_{\text{int}}}V_{\text{in}}(t) * [u(t) - u(t - t_{\text{int}})]. \quad (26)$$

Performing Laplace transformation

$$V_{\text{out}}(s) + \frac{V_{\text{out}}(s)}{C_{\text{int}}R_{\text{out}}}\left[\frac{1}{s} - \frac{e^{-st_{\text{int}}}}{s}\right] = \frac{G_m}{C_{\text{int}}}V_{\text{in}}(s)\left[\frac{1}{s} - \frac{e^{-st_{\text{int}}}}{s}\right] \quad (27)$$

$$H_{\text{GmC}}(s) = \frac{V_{\text{out}}(s)}{V_{\text{in}}(s)} = \frac{\text{GmR}_{\text{out}}(1 - e^{-st_{\text{int}}})}{1 - e^{-st_{\text{int}}} + R_{\text{out}}sC_{\text{int}}}. \quad (28)$$

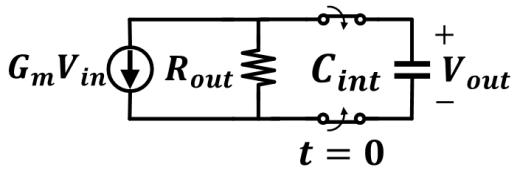

Fig. 33. Start of integration.

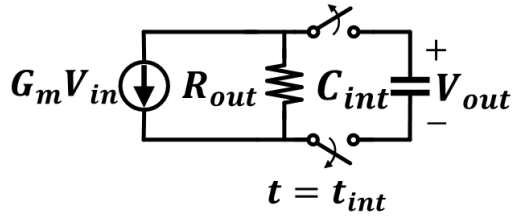

Fig. 34. Finish of integration.

For an ideal Gm-C integrator, the output resistance R_{out} approaches infinity, and (28) becomes

$$H_{\text{GmC}}(s) = \frac{G_m(1 - e^{-st_{\text{int}}})}{sC_{\text{int}}}. \tag{29}$$

The magnitude of its transfer function is given by

$$|H_{G_mC}(j\omega)| = \left|\frac{G_m(1 - e^{-j\omega t_{\text{int}}})}{C_{\text{int}} j\omega}\right| = \frac{2G_m \sin\left(\frac{\omega t_{\text{int}}}{2}\right)}{C_{\text{int}}\omega}$$

which can also be expressed as follows:

$$|H_{G_mC}(j2\pi f)| = \frac{G_m t_{\text{int}}}{C_{\text{int}}} \cdot \frac{\sin(t_{\text{int}}\pi f)}{t_{\text{int}}\pi f}. \tag{30}$$

The above equation predicts the transfer function of an ideal Gm-C integrator to be a sinc function with the dc gain of $G_m t_{\text{int}}/C_{\text{int}}$ and the first null bandwidth of $1/t_{\text{int}}$. It follows that, to have a higher signal gain, the Gm-C integrator should be designed to have a higher G_m and a lower C_{int} for a fixed integration time t_{int}. On the other hand, for a fixed G_m and C_{int}, longer integration time t_{int} also gives a higher gain and a lower bandwidth at the same time. The transfer function of an ideal Gm-C integrator (30) is plotted in Fig. 26(a), in contrast with a practical Gm-C integrator with a finite output resistance R_{out} in Fig. 26(b).

When a practical Gm-C integrator integrates for long enough time ($|e^{-st_{\text{int}}}| \ll 1$), (28) can be approximated as follows:

$$H_{\text{GmC}}(s) \approx \frac{G_m R_{\text{out}}}{1 + R_{\text{out}} s C_{\text{int}}} \tag{31}$$

which predicts a dc gain of $A_{V,\text{GmC}} = G_m R_{\text{out}}$ and a 3-dB bandwidth of $f_{3\,\text{dB}} = 1/(2\pi R_{\text{out}} C_{\text{int}})$. Comparing with (30), R_{out} sets the limits for the dc gain and the bandwidth, which can no longer be improved by longer integration time, which is shown in Fig. 26(b) and results in the saturation behaviors of the signal and noise in Fig. 16.

ACKNOWLEDGMENT

The authors would like to thank the Center for Nano and Micro Manufacturing (CNM2), University of California at Davis (UC Davis), Davis, CA, USA, and the Physics Department, UC Davis FIT, for technical support during the sensor fabrication and packaging, and Minji Zhu from Center for High Frequency Electronics (CHFE), University of California at Los Angeles (UCLA), Los Angeles, CA, USA, for the system wire bonding service.

REFERENCES

[1] K. Entesari, A. A. Helmy, and M. Moslehi-Bajestan, "Integrated systems for biomedical applications: Silicon-based RFmicrowave dielectric spectroscopy and sensing," *IEEE Microw. Mag.*, vol. 18, no. 5, pp. 57–72, Jul. 2017.

[2] D. Kissinger, M. Kaynak, and A. Mai, "Integrated millimeter-wave and terahertz analyzers for biomedical applications," *IEEE Trans. Microw. Theory Techn.*, vol. 70, no. 11, pp. 5141–5158, Nov. 2022.

[3] B. Yu, X. Ding, H. Yu, Y. Ye, X. Liu, and Q. J. Gu, "Ring-resonator-based sub-THz dielectric sensor," *IEEE Microw. Wireless Compon. Lett.*, vol. 28, no. 11, pp. 969–971, Nov. 2018.

[4] M. M. Bajestan, A. A. Helmy, H. Hedayati, and K. Entesari, "A 0.62–10 GHz complex dielectric spectroscopy system in CMOS," *IEEE Trans. Microw. Theory Techn.*, vol. 62, no. 12, pp. 3522–3537, Dec. 2014.

[5] M. Elkholy and K. Entesari, "A wideband low-power LC-DCO-based complex dielectric spectroscopy system in 0.18-μm CMOS," *IEEE Trans. Microw. Theory Techn.*, vol. 65, no. 11, pp. 4461–4474, Nov. 2017.

[6] M. Bakhshiani, M. A. Suster, and P. Mohseni, "A broadband sensor interface IC for miniaturized dielectric spectroscopy from MHz to GHz," *IEEE J. Solid-State Circuits*, vol. 49, no. 8, pp. 1669–1681, Aug. 2014.

[7] E. Kaya, A. P. Saghati, and K. Entesari, "A 3–10-GHz CMOS time-domain complex dielectric spectroscopy system using a contactless sensor," *IEEE Trans. Microw. Theory Techn.*, vol. 67, no. 12, pp. 5202–5217, Dec. 2019.

[8] F. I. Jamal, S. Guha, M. H. Eissa, J. Wessel, and D. Kissinger, "A fully integrated low-power 30 GHz complex dielectric sensor in a 0.25-μm BiCMOS technology," *IEEE J. Electromagn., RF Microw. Med. Biol.*, vol. 2, no. 3, pp. 163–171, Sep. 2018.

[9] B. Laemmle, K. Schmalz, J. C. Scheytt, R. Weigel, and D. Kissinger, "A 125-GHz permittivity sensor with read-out circuit in a 250-nm SiGe BiCMOS technology," *IEEE Trans. Microw. Theory Techn.*, vol. 61, no. 5, pp. 2185–2194, May 2013.

[10] J.-C. Chien and A. M. Niknejad, "Oscillator-based reactance sensors with injection locking for high-throughput flow cytometry using microwave dielectric spectroscopy," *IEEE J. Solid-State Circuits*, vol. 51, no. 2, pp. 457–472, Feb. 2016.

[11] H. Yu, B. Yu, X. Ding, J. S. Gómez-Díaz, and Q. J. Gu, "A 162 GHz ring resonator based high resolution dielectric sensor," in *IEEE MTT-S Int. Microw. Symp. Dig.*, Aug. 2020, pp. 233–236.

[12] A. P. Saghati, J. S. Batra, J. Kameoka, and K. Entesari, "A metamaterial-inspired wideband microwave interferometry sensor for dielectric spectroscopy of liquid chemicals," *IEEE Trans. Microw. Theory Techn.*, vol. 65, no. 7, pp. 2558–2571, Jul. 2017.

[13] J.-C. Chien, "A 1.8-GHz near-field dielectric plethysmography heart-rate sensor with time-based edge sampling," *IEEE J. Solid-State Circuits*, vol. 55, no. 3, pp. 615–628, Mar. 2020.

[14] X. Fan, I. M. White, S. I. Shopova, H. Zhu, J. D. Suter, and Y. Sun, "Sensitive optical biosensors for unlabeled targets: A review," *Analytica Chim. Acta*, vol. 620, nos. 1–2, pp. 8–26, Jul. 2008.

[15] F. Vollmer and S. Arnold, "Whispering-gallery-mode biosensing: Label-free detection down to single molecules," *Nature Methods*, vol. 5, no. 7, pp. 591–596, Jul. 2008.

[16] H. Yu, X. Ding, J. Chen, S. S. Saber, and Q. J. Gu, "A CMOS 160 GHz integrated permittivity sensor with resolution of 0.05% $\Delta\epsilon_r$," in *Proc. IEEE Radio Freq. Integr. Circuits Symp. (RFIC)*, Jun. 2023, pp. 245–248.

[17] S. Arnold and S. I. Shopova, "Whispering gallery mode biosensor," in *Biophotonics: Spectroscopy, Imaging, Sensing, and Manipulation*, B. D. Bartolo and J. Collins, Eds. Dordrecht, The Netherlands: Springer, 2011, pp. 237–259.

[18] B. Yu, Y. Liu, Y. Ye, X. Liu, and Q. J. Gu, "Low-loss and broadband G-band dielectric interconnect for chip-to-chip communication," *IEEE Microw. Wireless Compon. Lett.*, vol. 26, no. 7, pp. 478–480, Jul. 2016.

[19] K. Qian et al., "Under-coupling whispering gallery mode resonator applied to resonant micro-optic gyroscope," *Sensors*, vol. 17, no. 12, p. 100, Jan. 2017. [Online]. Available: https://www.mdpi.com/1424-8220/17/1/100

[20] S. Hao, T. Hu, and Q. J. Gu, "A 10-GHz delay line frequency discriminator and PD/CP-based CMOS phase noise measurement circuit," *IEEE Trans. Microw. Theory Techn.*, vol. 65, no. 7, pp. 2361–2372, Jul. 2017.
[21] S. A. Ahmadi-Mehr, M. Tohidian, and R. B. Staszewski, "Analysis and design of a multi-core oscillator for ultra-low phase noise," *IEEE Trans. Circuits Syst. I, Reg. Papers*, vol. 63, no. 4, pp. 529–539, Apr. 2016.
[22] R. Kananizadeh and O. Momeni, "High-power and high-efficiency millimeter-wave harmonic oscillator design, exploiting harmonic positive feedback in CMOS," *IEEE Trans. Microw. Theory Techn.*, vol. 65, no. 10, pp. 3922–3936, Oct. 2017.
[23] A. Ghorbani-Nejad, A. Nikpaik, A. Nabavi, A. H. M. Shirazi, S. Mirabbasi, and S. Shekhar, "Optimum conditions for efficient second-harmonic power generation in mm-wave harmonic oscillators," *IEEE J. Solid-State Circuits*, vol. 57, no. 7, pp. 2130–2142, Jul. 2022.
[24] X. Yi, C. C. Boon, H. Liu, J. F. Lin, and W. M. Lim, "A 57.9-to-68.3 GHz 24.6 mW frequency synthesizer with in-phase injection-coupled QVCO in 65 nm CMOS technology," *IEEE J. Solid-State Circuits*, vol. 49, no. 2, pp. 347–359, Feb. 2014.
[25] G. Vlachogiannakis, M. A. P. Pertijs, M. Spirito, and L. C. N. de Vreede, "A 40-nm CMOS complex permittivity sensing pixel for material characterization at microwave frequencies," *IEEE Trans. Microw. Theory Techn.*, vol. 66, no. 3, pp. 1619–1634, Mar. 2018.
[26] C. Adamopoulos et al., "Fully integrated electronic-photonic sensor for label-free refractive index sensing in advanced zero-change CMOS-SOI process," in *Proc. IEEE Custom Integr. Circuits Conf. (CICC)*, Apr. 2021, pp. 1–2.

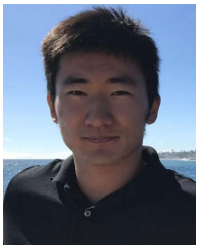

Hai Yu (Member, IEEE) received the B.S. degree in mechatronics engineering from the Beijing Institute of Technology, Beijing, China, in 2013, and the M.S. degree in electrical engineering from The Ohio State University, Columbus, OH, USA, in 2015. He is currently pursuing the Ph.D. degree in electrical engineering at the University of California at Davis, Davis, CA, USA.

His research interests include sub-THz sensing and transceivers.

Mr. Yu was a first-author recipient of the Best Student Paper Award of the 2020 IEEE International Microwave Symposium (IMS).

Xuan Ding (Member, IEEE) received the B.S. and M.S. (Hons.) degrees in electrical engineering from the University of Electronic Science and Technology of China (UESTC), Chengdu, China, in 2010 and 2013, respectively. He is currently pursuing the Ph.D. degree in electrical engineering at the University of California at Davis (UC Davis), Davis, CA, USA.

He is currently with the High Speed Integrated Circuits and Systems Laboratory, UC Davis. His research interests include RF, microwave, and THz-integrated circuits and systems.

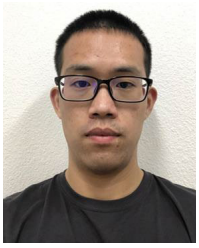

Jingjun Chen (Member, IEEE) received the B.S. degree in electronic science and technology from the Harbin Institute of Technology, Weihai, China, in 2016, and the Ph.D. degree in electrical and computer engineering from the University of California at Davis (UC Davis), Davis, CA, USA, in 2022.

He is currently working with Qualcomm Atheros Inc., Santa Clara, CA, USA, on RF transceiver IC for wireless communications. His research interests include millimeter-wave signal sources, amplifiers, transceivers, RF, microwave, and THz-integrated circuits and systems.

Sajjad Sabbaghi (Graduate Student Member, IEEE) received the B.S. degree in electronic engineering from Kashan University, Kashan, Iran, in 2015, and the master's degree in electronic engineering (IC design) from the K. N. Toosi University of Technology, Tehran, Iran, in 2018. He is currently pursuing the Ph.D. degree at the High-Speed Integrated Circuits and Systems Laboratory, University of California at Davis, Davis, CA, USA.

His research interests include millimeter-wave-integrated circuit design for sensing and communication applications.

Qun Jane Gu (Senior Member, IEEE) received the Ph.D. degree from the University of California at Los Angeles, Los Angeles, CA, USA, in 2007.

She is currently a Professor at the University of California at Davis, Davis, CA, USA. Her research interests include high efficiency, low-power interconnect, millimeter wave, and sub-mm-wave/terahertz-integrated circuits and systems for communication, radar, and imaging.

Dr. Gu is a TPC Member of solid-state circuits conferences, such as RFIC, CICC, and ISSCC. She was a recipient of the NSF CAREER award, the 2015 UC Davis Outstanding Junior Faculty Award, the 2017 and 2018 Qualcomm Faculty Award, the 2019 UC Davis Chancellor's Fellow, and the 2022–2023 IEEE Solid-State Circuits Society (SSCS) Distinguished Lecturer. Her group has got nine best paper awards from various international conferences. She was in the Steering Committee of IMS2016. She has been an Associate Editor of IEEE MICROWAVE AND WIRELESS COMPONENTS LETTERS (MWCL) and *VLSI Journal of Integration*, and a Guest Editor of IEEE JOURNAL OF SOLID-STATE CIRCUITS (JSSC) and IEEE TRANSACTIONS ON MICROWAVE THEORY AND TECHNIQUES (TMTT).